IEEE Access
Multidisciplinary ⋮ Rapid Review ⋮ Open Access Journal

Received 19 January 2023, accepted 16 February 2023, date of publication 27 February 2023, date of current version 2 March 2023.

Digital Object Identifier 10.1109/ACCESS.2023.3249219

RESEARCH ARTICLE

An Extended Frequency Scaling Algorithm for Bistatic SAR With High Squint Angle

HAOHUA ZHANG, WEIHUA ZUO, BO LIU, CAIPIN LI, DONGTAO LI, AND CHONGDI DUAN
Xi'an Branch, China Academy of Space Technology, Xian 710000, China

Corresponding author: Haohua Zhang (1402121299@stu.xidian.edu.cn)

ABSTRACT Bistatic synthetic aperture radar (BiSAR) is an extended and complementary observation method to conventional monostatic SAR remote sensing. When high range and azimuth resolution are required in BiSAR, the transmitting platform, i.e., the LEO satellite, should work in the spotlight or sliding spotlight mode, which means a wide bandwidth Chirp signal is transmitted, and the targets are illuminated for a long enough time as well. In order to reduce the sampling frequency in the receiving system and improve the efficiency of the focusing procedure for this BiSAR configuration, the echoes should be dechirp received. A bistatic extended frequency scaling algorithm (Bi-EFSA) is proposed in this paper to deal with the dechirp received bistatic SAR echoes. The first step of Bi-EFSA is the range walk correction in the 2-D time domain, which reduces the space variance of the range curvatures and removals the serious coupling between range and azimuth caused by the high squint angle. After that, the range compression is achieved by secondary range compression (SRC) and bulk shift. Then, the space variance of the azimuth frequency modulation rate, introduced by the range walk correction step, is corrected by implementing the azimuth nonlinear chirp scaling (ANCS) operation. Following this, the focused results in the range frequency and azimuth time domain are obtained by the azimuth compression. The point targets and extended-scene simulations validate the effectiveness of the proposed algorithm.

INDEX TERMS Bistatic SAR, high squint angle, dechirp received, bistatic extended frequency scaling algorithm, azimuth nonlinear chirp scaling.

I. INTRODUCTION

Bistatic synthetic aperture radar (BiSAR) is an extended and complementary observation method to conventional monostatic SAR remote sensing [1]. For the BiSAR, the transmitter can be settled on different types of platforms, such as airplanes, un-manned aerial vehicles (UAVs), LEO, MEO, and GEO satellites, while the receiver is mounted on airplanes or UAVs. The transmitter-receiver separated configuration offers more observation possibilities and design flexibility for remote sensing systems, which does not affect the observation of the monostatic SAR itself [2], [3]. Furthermore, its various viewing directions provide more scattering characteristics of complex objects, among which arouses intensive interest in key region observations and surveillance [4], [5], [6].

The associate editor coordinating the review of this manuscript and approving it for publication was Jiafeng Xie.

When high range and azimuth resolution are required at the same time in BiSAR, the transmitting platform, i.e., the LEO satellite, should work in the spotlight or sliding spotlight mode, which means a wide bandwidth Chirp signal is transmitted, and the targets are illuminated for a long enough time as well. In some observation tasks, i.e., key region imaging, the receiver must work with high squint angle instead of the side looking [7]. To reduce the sampling frequency in the receiving system and improve the efficiency of the focusing procedure for such a BiSAR configuration, the echoes should be dechirp received [8]. Also, the imaging algorithm should be able to removal the significant coupling between the range and the azimuth caused by the high squint angle.

The present BiSAR imaging algorithms fall into two broad categories: the time domain algorithms, i.e., the back-projection algorithm (BPA) [9], [10], [11]; and the

frequency domain algorithms, which include the range-Doppler algorithm (RDA) [12], [13], the chirp scaling algorithm (CSA) [14], [15], the nonlinear chirp scaling algorithm (NLCSA) [16], [17], [18], [19], [20], [21], the wave number domain algorithm (ωKA) [22], [23], [24], the frequency scaling algorithm (FSA) [25], and Space-Surface Bistatic SAR (SS-BiSAR) image formation algorithm [26]. The RDA simplifies imaging processing into two one-dimensional pulse compression processes by decoupling distance and azimuth processing under certain conditions. The RCM of different targets is corrected in the range-Doppler domain by interpolation. The CS algorithm is based on the scaling principle to modulate the frequency of the chirp signal. The RCM correction is completed by phase multiplication instead of interpolation in the time domain. The ωKA achieves uniform focusing by multiplying the two-dimensional matched filter function of the reference range after 2-D Fourier transform of the SAR echo data. The correction of the spatial-variant RCM, the range-azimuth coupling, and the azimuth compression are completed by supplementing the Stolt interpolation in 2-D frequency domain. However, the traditional BPA, RDA, NLCS, and ωKA lacks imaging efficiency because of interpolation operations. In addition, the RDA, CSA, NLCS, and ωKA cannot process the dechirp received echo.

The FS algorithm is utilized to process the dechirp received signal but cannot be applied to the BiSAR with high squint angle. FS algorithm is first proposed in [27], which is used for monostatic spotlight SAR data processing. In [25], the FS algorithm is extended to Bistatic Spotlight SAR configuration, in which the transmitter and receiver are assumed to operate in parallel and at equal speed. Based on an exact analytical bistatic point target spectrum obtained by a geometry-based formula (GBF) method, [28] used the FS algorithm in tandem configuration Bistatic SAR. To reduce the spectrum shift caused by the range scaling operation, the Extended frequency scaling algorithm (EFSA) is proposed in [29]. Compared to the FSA, the EFSA is more competent in large-squint applications. Deep research into the EFS algorithm for nonequal operating velocities of transmitter and receiver in a general bistatic configuration with high squint angles is worthy of deep analysis. The SS-BiSAR image formation algorithm in [26] processes the dechirp received signal with the transmitter-receiver direct signal as a reference. But, the transmitter-receiver direct signal is significantly inconsistent with the echo characteristics of the scene, which leads to inaccurate focusing results.

In this paper, a bistatic extended frequency scaling algorithm (Bi-EFSA) is proposed to deal with the dechirp received bistatic SAR echoes with high squint angle. Instead of the transmitter-receiver direct signal, the echo of the imaging scene centroid is used as the reference signal. The first step of Bi-EFSA is the range walk correction in the 2-D time domain, which corrects the linear component of range migration and removals the serious coupling between range and azimuth caused by the high squint angle. After that, the range compression is achieved by SRC and bulk shift. Then, the space variance of the azimuth frequency modulation rate, introduced by the range walk correction step, is corrected by implementing the azimuth nonlinear chirp scaling (ANCS) operation. Following this, the focused results in the range frequency and azimuth time domain are obtained by the azimuth compression. The proposed algorithm processes the dechirp received signal with the echo of the imaging scene centroid as the reference signal and implements the ANCS algorithm to achieve azimuth focusing. The algorithm can deal with the BiSAR with high squint angle and achieves good focusing performance and computational efficiency.

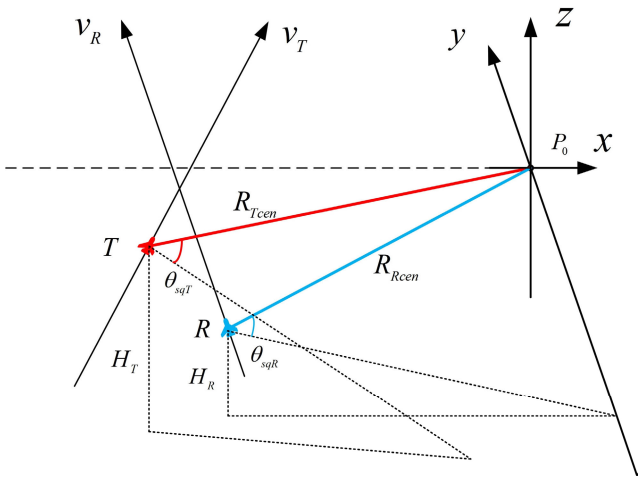

FIGURE 1. The configuration of the BiSAR with highly squinted angle.

The remainder of the paper is organized as follows. The echo model of BiSAR with high squint angles is introduced in Section II, and the dechirp received signal is also derived in this section. In Section III, the Bi-EFSA is introduced to deal with the dechirp received bistatic SAR echoes in details. The point targets simulations and the extended-scene simulations of BiSAR with high squint angles imaging are employed to validate the proposed algorithm in Section IV. Finally, the conclusion is drawn in Section V.

II. SIGNAL MODEL

The considered bistatic imaging geometry is showed in Figure 1. The transmitter and receiver platforms travel along their own moving directions at the altitudes of H_T and H_R with constant velocities v_T and v_R. The shortest slant ranges for them to the reference point P_0 (which is also the original point of the scene) are R_{Tcen} and R_{Rcen}. The $x-y$ plane is locally tangent to the Earth's surface by using the righthand Cartesian coordinate system. The reference point target P_0 is in the imaging plane $x-y$, which is also set to be the origin of the coordinates. θ_{sqT} and θ_{sqR} are the squint angles for P_0 at the azimuth zero time. P is an arbitrary point of the imaging area, which is nearby the P_0.

According to Figure.1, the instantaneous slant range of an arbitrary target is obtained as

$$\begin{aligned} &R(\eta) \\ &= R_T(\eta) + R_R(\eta) \\ &= \sqrt{V_T^2(\eta-\eta_0)^2 + R_{T0}^2 - 2V_T(\eta-\eta_0)R_{T0}\sin(\theta_{sqT})} \\ &\quad + \sqrt{V_R^2(\eta-\eta_0)^2 + R_{R0}^2 - 2V_R(\eta-\eta_0)R_{R0}\sin(\theta_{sqR})} \end{aligned} \tag{1}$$

in which η is azimuth time, and can be expanded into Taylor series at η_0:

$$\begin{aligned} R(\eta) = R_0 + k_1(\eta-\eta_0) + k_2(\eta-\eta_0)^2 \\ + k_3(\eta-\eta_0)^3 + k_4(\eta-\eta_0)^4 + \ldots \end{aligned} \tag{2}$$

η_0 is the azimuth zero time for beam center crossing the reference target (i.e., the target with $\eta_0 = 0$). R_0 donates the sum of transmit slant range R_{T0} and receive slant range R_{R0} at the beam center crossing time. The derivative coefficients of each order are given in [30] and are all weakly associated with the azimuth and range of the target during the synthetic aperture time.

The received original echo signal from a point target after baseband demodulation can be express as

$$\begin{aligned} &s_0(\tau,\eta) \\ &= rect\left(\frac{\tau - \frac{R(\eta)}{c}}{T_p}\right) w(\eta) \exp\left\{j2\pi f_c\left(\tau - \frac{R(\eta)}{c}\right)\right\} \\ &\quad \cdot \exp\left\{j\pi K_r\left(\tau - \frac{R(\eta)}{c}\right)^2\right\} \end{aligned} \tag{3}$$

where τ is the fast time; T_p is the width of transmitted plus signal; $w(\eta)$ is the azimuth envelope given by the composite antenna pattern; f_c is the carry frequency; K_r is the range frequency modulation rate.

The dechirp operation can be achieved by utilizing a dechirp-receiver. After dechirp receiving, the range echo of the target turns into single frequency signal, which only relay to the difference between the slant range of the point target P, i.e., $R(\eta, R_0)$ and the reference range of P_0, i.e., R_{cen}. The reference signal for the dechirp-received is

$$\begin{aligned} &H_{dechirp} \\ &= \exp\left\{-j\pi K_r\left(\tau - \frac{R_{cen}}{c}\right)^2\right\} \exp\left\{-j2\pi f_c\left(\tau - \frac{R_{cen}}{c}\right)\right\} \end{aligned} \tag{4}$$

where $R_{cen} = R_{Tcen} + R_{Rcen}$ denotes the sum of the transmit and receive ranges between the scene central reference point and the synthetic aperture midpoint for bistatic SAR. The reference signal for dechirp receiving is derived and calculated based on the two-way slant ranges from the imaging scene centroid point to the transmitter and receiver, which significantly differs from that of the literature [26] and can help the consequent processing to get better focused results. Then, the dechirp-received signal expression of the arbitrary target is derived and given by

$$\begin{aligned} &s_1(\tau,\eta) \\ &= A rect\left(\frac{\tau - \frac{R(\eta,R_0)}{c}}{T_p}\right) \exp\left\{-j\frac{2\pi K_r}{c}\tau\left[R(\eta,R_0) - R_{cen}\right]\right\} \\ &\quad \cdot rect\left(\frac{\eta-\eta_0}{T_a}\right) \exp\left\{-j\frac{2\pi R(\eta,R_0)}{\lambda}\right\} \\ &\quad \cdot \exp\left\{j\frac{2\pi K_r}{c^2}R_{cen}\left[R(\eta,R_0) - R_{cen}\right]\right\} \\ &\quad \cdot \exp\left\{j\frac{\pi K_r}{c^2}\left[R(\eta,R_0) - R_{cen}\right]^2\right\} \end{aligned} \tag{5}$$

A is a complex constant, including the information on reflection coefficients of antennas and the ground; T_a is the synthetic aperture time. The range echo turns into single frequency signal after dechirp receiving, and the single frequency is $-K_s(R(\eta,R_0) - R_{cen})/c$. The dechirp received signal helps to reduce the sampling frequency in the receiving system and improve the efficiency of the focusing procedure for such a BiSAR configuration. The last term of (5) represents the residual video phase (RVP), which is generated in the process of dechirp and needs to be compensated. In the subsequent derivation, $R(\eta, R_0)$ is simply expressed as r.

III. BISTATIC EXTENDED FREQUENCY SCALING ALGORITHM (BI-EFSA)

The bistatic extended frequency scaling algorithm (Bi-EFSA) is proposed to deal with the dechirp received bistatic SAR echoes with high squint angle. The RWC is used in the 2-D time domain first, to reduce the linear component of range migration and removal the serious coupling between range and azimuth caused by the high squint angle. After that, the range compression is achieved by SRC and bulk shift. The ANCS method is implemented to correct the space variance of the azimuth frequency modulation rate, which is introduced by the range walk correction step. This section details the derivation and analysis of the Bi-EFSA for the bistatic high squint SAR.

A. RVP CORRECTION AND RANGE WALK CORRECTION

In the pre-processing stage, the RVP correction is completed. It is implemented in the fast time frequency domain and is known as the deskew operation. Then, multiply it by the deskew function as (6) after converting (5) to the fast time frequency domain.

$$H_{deskew} = \exp\left(-j\frac{\pi}{K_r}f_r^2\right) \tag{6}$$

After deskew operation, the signal is converted back to the fast time domain. It is worth noting that the center of the signal envelope in equation (7) has changed to r_{cen}/c.

$$\begin{aligned} &s_2(\tau,\eta) \\ &= A rect\left(\frac{\tau - \frac{r_{cen}}{c}}{T_p}\right) \exp\left\{-j\frac{2\pi}{\lambda}\left(1 + \frac{\lambda K_r}{c}\left(\tau - \frac{r_{cen}}{c}\right)\right) r\right\} \\ &\quad \cdot rect\left(\frac{\eta-\eta_0}{T_a}\right) \exp\left\{j\frac{2\pi K_r r_{cen}}{c}\left(\tau - \frac{r_{cen}}{c}\right)\right\} \end{aligned} \tag{7}$$

According to the double hyperbolic range expansion (2) and the signal $s_2(\tau,\eta)$, the range walk can be corrected by multiplying the RWC function in the 2-D time domain

$$\begin{aligned} &H_{RWC}(\tau,\eta) \\ &= \exp\left(j\frac{2\pi}{\lambda}\left(1+\frac{\lambda K_r}{c}\left(\tau-\frac{r_{cen}}{c}\right)\right)k_1\eta\right) \\ &= \exp\left(-j\frac{2\pi}{\lambda}\left(1+\frac{\lambda K_r}{c}\left(\tau-\frac{r_{cen}}{c}\right)\right)\right. \\ &\quad \left.\left(V_T\sin\theta_{sqT}+V_R\sin\theta_{sqR}\right)\eta\right) \end{aligned} \tag{8}$$

The signal after RWC can be expressed as

$$\begin{aligned} &s_3(\tau,\eta) \\ &\approx Arect\left(\frac{\tau-\frac{r_{cen}}{c}}{T_p}\right) \\ &\quad\times\exp\left\{-j\frac{2\pi}{\lambda}\left(1+\frac{\lambda K_r}{c}\left(\tau-\frac{r_{cen}}{c}\right)\right)(r-k_1\eta)\right\} \\ &\quad\cdot rect\left(\frac{\eta-\eta_0}{T_a}\right)\exp\left\{j\frac{2\pi K_r r_{cen}}{c}\left(\tau-\frac{r_{cen}}{c}\right)\right\} \end{aligned} \tag{9}$$

To derive the expression in the range Doppler domain of the signal, only the azimuth time phase expression needs to be considered:

$$\Phi(\eta)=-\frac{2\pi}{\lambda}\left(1+\frac{\lambda K_r}{c}\left(\tau-\frac{r_{cen}}{c}\right)\right)(r-k_1\eta)-2\pi f_\eta\eta \tag{10}$$

According to the POSP, azimuth frequency can be express as

$$\begin{aligned} &f_\eta(\eta) \\ &= -\frac{1}{\lambda}\left(1+\frac{\lambda K_r}{c}\left(\tau-\frac{r_{cen}}{c}\right)\right)(r-k_1\eta)' \\ &= -\frac{1}{\lambda}\left(1+\frac{\lambda K_r}{c}\left(\tau-\frac{r_{cen}}{c}\right)\right) \\ &\quad\times\begin{pmatrix}2k_2(\eta-\eta_0)\\+3k_3(\eta-\eta_0)^2+4k_4(\eta-\eta_0)^3\end{pmatrix} \end{aligned} \tag{11}$$

In order to relate the azimuth time η and the azimuth frequency f_η, the coefficients of the inverse function are calculated from the coefficients of the given function as follows [16], [30]

$$\begin{aligned} f_\eta(\eta) &= a_1(\eta-\eta_0)+a_2(\eta-\eta_0)^2+a_3(\eta-\eta_0)^3 \\ \eta(f_\eta)-\eta_0 &= A_1f_\eta+A_2f_\eta^2+A_3f_\eta^3+\cdots \end{aligned}$$

where

$$\begin{aligned} a_1 &= -\frac{2K}{\lambda}k_2, \quad a_2=-\frac{3K}{\lambda}k_3, \quad a_3=-\frac{4K}{\lambda}k_4 \\ A_1 &= -\frac{\lambda}{2K}k_2^{-1}, \quad A_2=-\frac{3\lambda^2}{8K^2}k_2^{-3}k_3, \\ A_3 &= -\frac{\lambda^3}{16K^3}k_2^{-5}\left(9k_3^2-4k_2k_4\right) \\ K &= 1+\frac{\lambda K_r}{c}\left(\tau-\frac{r_{cen}}{c}\right) \end{aligned}$$

The phase function of f_η can be derived as

$$\begin{aligned} \Phi(f_\eta) &= \Phi(\eta(f_\eta)) \\ &= -\frac{2\pi}{\lambda}K\begin{pmatrix}R_0-k_1\eta_0+k_2(\eta-\eta_0)^2\\+k_3(\eta-\eta_0)^3+k_4(\eta-\eta_0)^4\end{pmatrix}-2\pi f_\eta\eta \\ &= -\frac{2\pi}{\lambda}K\cdot(R_0-k_1\eta_0)+2\pi f_\eta\eta_0+\frac{\pi\lambda}{2K}\frac{1}{k_2}f_\eta^2+\ldots \\ &\quad\ldots+\frac{\pi\lambda^2}{4K^2}\frac{k_3}{k_2^3}f_\eta^3-\frac{\pi\lambda^3}{8K^3}\frac{1}{k_2^4}\left(k_4-\frac{9k_3^2}{4k_2}\right)f_\eta^4 \end{aligned} \tag{12}$$

Obviously, the phase function is difficult to express as a function of τ directly. Thus, expanding (12) in Talyor series at $\tau=r_{cen}/c$ is crucial for the subsequent analysis.

$$\begin{aligned} &\Phi(\tau,f_\eta;R_0) \\ &= \phi_0(f_\eta,R_0)+\phi_1(f_\eta,R_0)\left(\tau-\frac{r_{cen}}{c}\right) \\ &\quad+\phi_2(f_\eta,R_0)\left(\tau-\frac{r_{cen}}{c}\right)^2 \\ &\quad+\phi_3(f_\eta,R_0)\left(\tau-\frac{r_{cen}}{c}\right)^3+\phi_4(f_\eta,R_0)\left(\tau-\frac{r_{cen}}{c}\right)^4 \end{aligned} \tag{13}$$

The coefficients in (13) are shown in (14), as shown at the bottom of the next page. The constant term represents the azimuth modulation, the prominent expression of azimuth processing. The first-order phase term corresponds to the residual range migration, which is reflected in the range frequency domain because of the dechirp received. After the RWC, the range curvature is the major component of the range migration and is space variance. The quadratic phase term represents the SRC term. The cubic and quartic terms represent the third- and fourth-order phase terms.

The fourth-order phase term is omitted and will be discussed in the Results Section. Priority can be given to compensating the third-order phase term for the subsequent FS operation and secondary range compression. Based on the results of the expansion calculation of the phase term described above, the third-order phase term is compensated as follows

$$H_{3\mathrm{rd}}(\tau,f_\eta)=\exp\left(-j\phi_3(f_\eta,R_0)\left(\tau-\frac{r_{cen}}{c}\right)^3\right) \tag{15}$$

The signal after compensated is as

$$\begin{aligned} &s_4(\tau,f_\eta) \\ &= A'\exp\left\{j\phi_0(f_\eta,R_0)\right\}\exp\left\{j\phi_1(f_\eta,R_0)\left(\tau-\frac{r_{cen}}{c}\right)\right\} \\ &\quad\cdot\exp\left\{j\phi_2(f_\eta,R_0)\left(\tau-\frac{r_{cen}}{c}\right)^2\right\} \\ &\quad\times\exp\left\{j\frac{2\pi K_r r_{cen}}{c}\left(\tau-\frac{r_{cen}}{c}\right)\right\} \end{aligned} \tag{16}$$

where A' is related to A and constant term resulted from POSP. The range and azimuth envelop are ignored for simplicity.

B. FREQUENCY SCALING

According to the study in Subsection III. A., the range curvature is space variance. To correct the range curvatures of all targets at once, the space variance must be reduced, which can be achieved by using the frequency scaling (FS) operation in the two-dimension frequency domain.

After the RWC and third-order phase compensation, the third and fourth-order phase terms of the signal equation (13) are small enough to be neglected during the conversion to the two-dimension frequency domain. This can be verified by numerical simulation.

By using POSP, the signal in two-dimension frequency is derived, and the range and azimuth envelop are ignored for simplicity.

$$\begin{aligned} S_4\left(f_\tau, f_\eta\right) = & \exp\left\{j\phi_0\left(f_\eta, R_0\right)\right\} \\ & \cdot \exp\left\{-j\frac{\pi}{K_m}\left[f_\tau - \left(f_s + \frac{K_r r_{cen}}{c}\right)\right]^2\right\} \\ & \times \exp\left\{-j2\pi\frac{r_{cen}}{c}f_\tau\right\} \end{aligned} \tag{17}$$

where (18), as shown at the bottom of the next page, K_m represents range frequency modulation rate after RWC; f_s is the position of the point target in range frequency domain. For different range sampling points, ΔR denotes the difference value of the transmit and receive slant ranges at azimuth zero time relative to the reference point in the scene center. Then, ΔR can be represented as $\Delta R = R_0 - r_{cen} = R_{T0} + R_{R0} - R_{Tcen} - R_{Rcen}$. In the bistatic SAR configuration, ϕ_0, ϕ_1, and ϕ_2 are space variances as was discussed previously, and it is difficult to obtain their analytical expressions regarding ΔR (essentially the analytic expressions of $1/k_2$, k_3/k_2^3 and $\left(k_4 - 9k_3^2/4k_2\right)/k_2^4$ regarding ΔR). Firstly, in the center of the scene, place a fixed number of point targets at equal intervals along the range and calculate the slant range at zero slow time for each point target $R_{Tcen} + R_{Rcen}$. The ΔR corresponding to each point target is obtained. Then, the coefficients $1/k_2$, k_3/k_2^3 and $\left(k_4 - 9k_3^2/4k_2\right)/k_2^4$ corresponding to each point target are calculated separately.

TABLE 1. Experiment parameters for airborne BiSAR.

Simulation Paraments	Transmitter	Receiver
Altitude	3000 m	2000 m
Velocity	262 m/s	200 m/s
Yaw angle	37°	0°
Squint angle	68°	40°
Center frequency	5.3 GHz	
Range Bandwidth	80 MHz	
Transmitted pulse duration	10 μs	
PRF	1200	

Lastly, a quadratic curve was fitted based on the calculated results relative to the numerical relationship of ΔR.

$$\begin{aligned} 1/k_2 &= m_0 + m_1\Delta R + m_2\Delta R^2 \\ k_3/k_2^3 &= l_0 + l_1\Delta R + l_2\Delta R^2 \\ \left(k_4 - 9k_3^2/4k_2\right)/k_2^4 &= q_0 + q_1\Delta R + q_2\Delta R^2 \end{aligned} \tag{19}$$

Substituting the expansions into equation (14), the analytical expressions for ϕ_0, ϕ_1, and ϕ_2 in terms of ΔR are obtained. And the expressions for ϕ_1 and f_s are as

$$\begin{aligned} \phi_1\left(f_\eta, \Delta R\right) = & 2\pi f_s = 2\pi \cdot \\ & -\frac{K_r}{c}\left(A(f_\eta) + B(f_\eta)\Delta R + C(f_\eta)\Delta R^2\right) \end{aligned} \tag{20}$$

where

$$\begin{aligned} A(f_\eta) &= (R_0 + k_1\eta_0) + \frac{\lambda^2}{4}m_0 f_\eta^2 + \frac{\lambda^3}{4}l_0 f_\eta^3 - \frac{3\lambda^4}{16}q_0 f_\eta^4 \\ B(f_\eta) &= \frac{\lambda^2}{4}m_1 f_\eta^2 + \frac{\lambda^3}{4}l_1 f_\eta^3 - \frac{3\lambda^4}{16}q_1 f_\eta^4 \\ C(f_\eta) &= \frac{\lambda^2}{4}m_2 f_\eta^2 + \frac{\lambda^3}{4}l_2 f_\eta^3 - \frac{3\lambda^4}{16}q_2 f_\eta^4 \end{aligned} \tag{21}$$

Based on the simulation parameters listed in Table 1, the simulation results of coefficients $A(f_\eta)$, $B(f_\eta)$ and $C(f_\eta)$ are given in the Figure 2. When the image width is small, $C(f_\eta)$ is insignificant and the phase $-2\pi K_r/c \cdot \left(C(f_\eta)\Delta R^2\right)$ is less than $\pi/4$. $C(f_\eta)$ can be ignored. The proposed algorithm takes

$$\begin{cases} \phi_0\left(f_\eta, R_0\right) = -\frac{2\pi}{\lambda}\left(R_0 - k_1\eta_0\right) - 2\pi f_\eta\eta_0 + \frac{\pi\lambda}{2}\frac{1}{k_2}f_\eta^2 + \frac{\pi\lambda^2}{4}\frac{k_3}{k_2^3}f_\eta^3 - \frac{\pi\lambda^3}{8}\frac{1}{k_2^4}\left(k_4 - \frac{9k_3^2}{4k_2}\right)f_\eta^4 \\ \phi_1\left(f_\eta, R_0\right) = -\frac{2\pi K_r}{c}\left(R_0 - k_1\eta_0\right) - \frac{\pi\lambda^2 K_r}{2c}\frac{1}{k_2}f_\eta^2 - \frac{\pi\lambda^3 K_r}{2c}\frac{k_3}{k_2^3}f_\eta^3 + \frac{3\pi\lambda^4 K_r}{8c}\frac{1}{k_2^4}\left(k_4 - \frac{9k_3^2}{4k_2}\right)f_\eta^4 \\ \qquad\qquad \triangleq 2\pi f_s \\ \phi_2\left(f_\eta, R_0\right) = \frac{\pi\lambda^3 K_r^2}{2c^2}\frac{1}{k_2}f_\eta^2 + \frac{3\pi\lambda^4 K_r^2}{4c^2}\frac{k_3}{k_2^3}f_\eta^3 - \frac{3\pi\lambda^5 K_r^2}{4c^2}\frac{1}{k_2^4}\left(k_4 - \frac{9k_3^2}{4k_2}\right)f_\eta^4 \\ \qquad\qquad \triangleq \pi K_m \\ \phi_3\left(f_\eta, R_0\right) = -\frac{\pi\lambda^4 K_r^3}{2c^3}\frac{1}{k_2}f_\eta^2 - \frac{\pi\lambda^5 K_r^3}{c^3}\frac{k_3}{k_2^3}f_\eta^3 + \frac{5\pi\lambda^6 K_r^3}{4c^3}\frac{1}{k_2^4}\left(k_4 - \frac{9k_3^2}{4k_2}\right)f_\eta^4 \\ \phi_4\left(f_\eta, R_0\right) = \frac{\pi\lambda^5 K_r^4}{2c^4}\frac{1}{k_2}f_\eta^2 + \frac{5\pi\lambda^6 K_r^4}{4c^4}\frac{k_3}{k_2^3}f_\eta^3 - \frac{15\pi\lambda^7 K_r^4}{8c^4}\frac{1}{k_2^4}\left(k_4 - \frac{9k_3^2}{4k_2}\right)f_\eta^4 \end{cases} \tag{14}$$

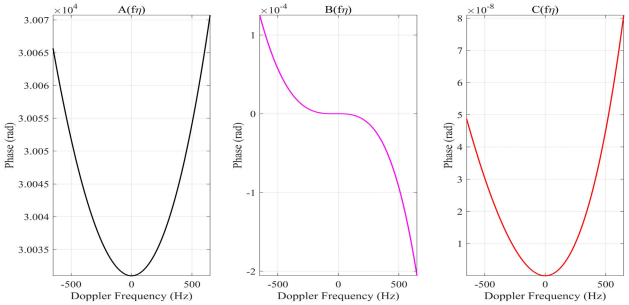

FIGURE 2. The simulation results of coefficients $A(f_\eta)$, $B(f_\eta)$ and $C(f_\eta)$.

quadratic curve fitting to obtain the numerical relationship of ΔR. Thus, the limitation of phase $-2\pi K_r/c\cdot\left(C(f_\eta)\Delta R^2\right)$ also determines the swath of imaging, which will be analyzed in Section III. *I*. Furthermore, if wide swath application is needed for proposed algorithm, new fitting method should be considered to obtain more accuracy results.

According to (17), $f_s + K_r r_{cen}/c$ denotes the target's location in range frequency domain; consequently, f_s' substitutes $f_s + K_r r_{cen}/c$. And f_s' is as

$$f_s' = f_s + \frac{k_r r_{cen}}{c} = -\frac{K_r}{c}\left[A'(f_\eta) + B'(f_\eta)\Delta R\right] \tag{22}$$

where

$$\begin{aligned} A'(f_\eta) &= k_1\eta_0 + \frac{\lambda^2}{4}m_0 f_\eta^2 + \frac{\lambda^3}{4}l_1 f_\eta^3 - \frac{3\lambda^4}{16}q_0 f_\eta^4 \\ B'(f_\eta) &= 1 + \frac{\lambda^2}{4}m_1 f_\eta^2 + \frac{\lambda^3}{4}l_1 f_\eta^3 - \frac{3\lambda^4}{16}q_1 f_\eta^4 \end{aligned} \tag{23}$$

Based on the idea of chirp scaling operation, the FS operation is applied in frequency domain. The FS operation modifies all migratory trajectories to be consistent with the scene's center target P_0 by correcting space variance of parameters such as f_s'. The above analysis demonstrates that the FS reference function is constructed using a point target migration factor to perform the scaling.

$$H_{FS}(f_\eta, f_\tau) = \exp\left\{-j\frac{\pi}{K_{merf}}\left(B'(f_\eta) - 1\right)\left(f_\tau - f_{ref}\right)^2\right\} \tag{24}$$

In the formula $f_{ref} = -K_r/c\cdot\left[A'(f_\eta) - k_1\eta_0\right]\big|_{\eta_0=0}$. Since $K_{merf} = K_m(f_\eta, R_0)$ is a space variance, we use the linear modulation frequency $K_{merf} = K_m(f_\eta, R_c)$ of the central reference point in the reference scene as an approximation.

After the FS operation, the two-dimension frequency domain expression of the echo signal is obtained as

$$\begin{aligned} S_5\left(f_\tau, f_\eta\right) = {} & A_3 \exp\left\{j\phi_0\left(f_\eta, R_0\right)\right\} \\ & \times \exp\left\{-j\frac{\pi}{K_{merf}}B'(f_\eta)\left(f_\tau - f_{fs}\right)^2\right\} \\ & \cdot \exp\left\{-j2\pi\frac{r_{cen}}{c}f_\tau\right\}\exp\left\{j\phi_{res}\left(f_\eta, R_0\right)\right\} \end{aligned} \tag{25}$$

in which $f_{fs} = -K_r/c\cdot\left(A'(f_\eta) + \Delta R\right)$. After FS operation, the range curvature is only related to the azimuth frequency and the reference slant range, and all point targets' echoes have the same amount of range curvature in the range frequency domain. Therefore, it is possible to correct the range curvature of all target points at once.

The FS operation introduces residual phase $\phi_{res}\left(f_\eta, R_0\right)$ as shown in (26), which will be compensated for after range compression.

$$\phi_{res}\left(f_\eta, R_0\right) = -\frac{\pi}{K_{mref}}B'(f_\eta)\left(B'(f_\eta) - 1\right)\left(\frac{K_r}{c}\Delta R\right)^2 \tag{26}$$

C. SECONDARY RANGE COMPRESSION AND BULK SHIFT

Secondary range compression and bulk shift will implement range compression and range curvature correction in the range Doppler domain. After the FS operation, the two-dimension frequency domain signal is converted to the range Doppler domain by using POSP and is as

$$\begin{aligned} & S_6\left(\tau, f_\eta\right) \\ & = A_4 \exp\left\{j\phi_0\left(f_\eta, R_0\right)\right\}\exp\left\{j\frac{\pi K_{merf}}{B'(f_\eta)}\left(\tau - \frac{r_{cen}}{c}\right)^2\right\} \\ & \quad \times \cdot \exp\left\{j2\pi f_{fs}\left(\tau - \frac{r_{cen}}{c}\right)\right\}\exp\left\{j\phi_{res}\left(f_\eta, R_0\right)\right\} \end{aligned} \tag{27}$$

The SRC and bulk shift transform function should be as follows.

$$\begin{aligned} H_{SRC+BV}\left(\tau, f_\eta\right) = {} & \exp\left\{-j\frac{\pi K_{merf}}{B'(f_\eta)}\left(\tau - \frac{r_{cen}}{c}\right)^2\right\} \\ & \times \exp\left\{-j2\pi f_{ref}\left(\tau - \frac{r_{cen}}{c}\right)\right\} \end{aligned} \tag{28}$$

(29) is obtained by multiplying (27) with the transform function and converting the multiplication results to the range frequency domain. B_r is transmit signal bandwidth.

$$\begin{aligned} & S_7\left(f_\tau, f_\eta\right) \\ & = A_4 \sin c\left\{B_r\left(f_r + \frac{K_r}{c}\Delta R\right)\right\} \\ & \quad \times \exp\left\{j\phi_0\left(f_\eta, R_0\right)\right\}\exp\left\{\phi_{res}\left(f_\eta, R_0\right)\right\} \end{aligned} \tag{29}$$

$$\begin{cases} K_m = \frac{\lambda^3 K_r^2}{2c^2}\frac{1}{k_2}f_\eta^2 + \frac{3\lambda^4 K_r^2}{4c^2}\frac{k_3}{k_2^3}f_\eta^3 - \frac{3\lambda^5 K_r^2}{4c^2}\frac{1}{k_2^4}\left(k_4 - \frac{9k_3}{4k_2}\right)f_\eta^4 \\ f_s = -\frac{K_r}{c}\left[\left(R_0 + k_1\eta_0\right) + \frac{\lambda^2}{4}\frac{1}{k_2}f_\eta^2 + \frac{\lambda^3}{4}\frac{k_3}{k_2^3}f_\eta^3 - \frac{3\lambda^4}{16}\frac{1}{k_2^4}\left(k_4 - \frac{9k_3^2}{4k_2}\right)f_\eta^4\right] \end{cases} \tag{18}$$

The residual phase compensation function is given by:

$$H_{rpc}(f_\eta, \Delta R) = \exp\left\{j\frac{\pi}{K_{merf}}\frac{B'(f_\eta)-1}{B'(f_\eta)}\left(f_s' - f_{ref}\right)^2\right\} \quad (30)$$

The range compressed signal is obtained after all the preceding processes.

$$S_8\left(f_\tau, f_\eta\right) = A_4 \sin c\left\{B_r\left(f_\tau + \frac{K_r}{c}\Delta R\right)\right\}\exp\left\{j\phi_0\left(f_\eta, R_0\right)\right\} \quad (31)$$

After the SRC and Bulk Shift operation, the trajectory becomes parallel to the azimuth frequency axis. The simulation results after FS operation are given in RESULTS section.

D. AZIMUTH FREQUENCY MODULATION ANALYSED

The targets are compressed to the corresponding range cells through range compression. And the focusing of the echoes in the azimuthal direction will be accomplished in next step. The signal obtained from the preceding processes is analyzed, and the azimuthal modulation is determined by $\phi_0\left(f_\eta, R_0\right)$.

$$\begin{aligned}\phi_0\left(f_\eta, R_0\right) = &-\frac{2\pi}{\lambda}\left(R_0 + k_1\eta_0\right) - 2\pi f_\eta\eta_0 - \frac{\pi\lambda}{2}\frac{1}{k_2}f_\eta^2 \\ &+ \frac{\pi\lambda^2}{4}\frac{k_3}{k_2^3}f_\eta^3 - \frac{\pi\lambda^3}{8}\frac{1}{k_2^4}\left(k_4 - \frac{9k_3^2}{4k_2}\right)f_\eta^4\end{aligned} \quad (32)$$

The signal expression is obtained by substituting $\phi_0\left(f_\eta, R_0\right)$ into the signal (31) and replacing the envelop with $P_r\left(f_\tau\right)$. For simplicity, replace A_4 with A, which is a complex constant.

$$\begin{aligned}S_8\left(f_\tau, f_\eta\right) = &AP_r\left(f_\tau\right)\exp\left\{-j2\pi f_\eta\eta_0\right\} \\ &\cdot \exp\left\{-j\frac{\pi\lambda}{2}\frac{1}{k_2}f_\eta^2\right\}\exp\left\{j\varphi_3 f_\eta^3\right\}\exp\left\{j\varphi_4 f_\eta^4\right\}\end{aligned} \quad (33)$$

in which

$$\begin{aligned}\varphi_3 &= \frac{\pi\lambda^2}{4}\frac{k_3}{k_2^3} \\ \varphi_4 &= -\frac{\pi\lambda^3}{8}\frac{1}{k_2^4}\left(k_4 - \frac{9k_3^2}{4k_2}\right)\end{aligned} \quad (34)$$

And the azimuth frequency modulation rate K_a is given by the second phase term of (33), which is azimuth-dependent after range compression. The K_a can be expressed and expanded as that in [19] and [20], $K_a = -2k_2/\lambda \approx K_{a0} + K_{a1}\eta_0$. K_{a0} is the frequency modulation at reference point in azimuth. While K_{a1} is the space variance of azimuth for frequency modulation, and it must be calibrated before the azimuth compression.

Despite the introduction of perturbation terms in the azimuth processing in the literature [16] and [31] to equalize the azimuth frequency modulation, this would cause geometric distortions in the azimuth, and additional interpolation would be required subsequently to correct the distortions, affecting the computational efficiency. The correction of azimuth frequency modulation and the azimuth focusing is achieved by ANCS, specifically including FFT and multiplication operations, which are more efficient.

E. HIGH ORDER AZIMUTH PHASE FILTER

Both the cubic and quadratic phases in equation (32) must be eliminated in ANCS processing since they cannot be ignored in the bistatic highly squint configuration. The high order phase filter is designed, in which Y_3 and Y_4 are undetermined.

$$H_{Fliter}\left(f_\tau, f_\eta\right) = \exp\left\{j\pi\left(Y_3 f_\eta^3 + Y_4 f_\eta^4\right)\right\} \quad (35)$$

Multiplying (33) with (35), we got filtered signal is as follow

$$\begin{aligned}&S_9\left(f_\tau, f_\eta\right) \\ &= AP_r\left(f_\tau\right)\exp\left\{-j2\pi f_\eta\eta_0\right\}\exp\left\{-j\frac{\pi\lambda}{2}\frac{1}{k_2}f_\eta^2\right\} \\ &\quad\cdot \exp\left\{j\left(\varphi_3 + Y_3\right)f_\eta^3\right\}\exp\left\{j\left(\varphi_4 + Y_4\right)f_\eta^4\right\}\end{aligned} \quad (36)$$

The signal in azimuth time domain is derived by converting (36):

$$\begin{aligned}S_9\left(f_\tau, \eta\right) = &AP_r\left(f_\tau\right)\exp\left\{j\pi K_a\left(\eta - \eta_0\right)^2\right\} \\ &\cdot \exp\left\{j\left(\varphi_3 + Y_3\right)K_a^3\left(\eta - \eta_0\right)^3\right\} \\ &\times \exp\left\{j\left(\varphi_4 + Y_4\right)K_a^4\left(\eta - \eta_0\right)^4\right\}\end{aligned} \quad (37)$$

F. ANCS OPERATION

The space variance of the azimuth modulation rate has been analyzed, which can be corrected by implementing the ANCS operation. The ANCS function is set as

$$H_{ANCS}\left(\eta\right) = \exp\left\{j\pi q_2\eta^2 + j\pi q_3\eta^3 + j\pi q_4\eta^4\right\} \quad (38)$$

Multiplying (37) with the ANCS chirp function and converting the results to the range Doppler domain with the principle of stationary phase (POSP), we got the signal expressed as

$$\begin{aligned}&S_{10}\left(f_\tau, f_\eta\right) \\ &= AP_r\left(f_\tau\right)\exp\left\{-j\frac{2\pi}{K_a + q_2}f_\eta\left(f_\eta + K_a\eta_0\right)\right\} \\ &\quad\cdot \exp\left\{j\frac{\pi}{\left(K_a + q_2\right)^2}\left[K_a\left(f_\eta - q_2\eta_0\right)^2 + q_2\left(f_\eta + K_a\eta_0\right)^2\right]\right\} \\ &\quad\cdot \exp\left\{j\frac{\pi}{\left(K_a + q_2\right)^3}\left[\left(\varphi_3 + Y_3\right)K_a^3\left(f_\eta - q_2\eta_0\right)^3\right.\right. \\ &\quad\left.\left. + q_3\left(f_\eta + K_a\eta_0\right)^3\right]\right\} \\ &\quad\cdot \exp\left\{j\frac{\pi}{\left(K_a + q_2\right)^4}\left[\left(\varphi_4 + Y_4\right)K_a^4\left(f_\eta - q_2\eta_0\right)^4\right.\right. \\ &\quad\left.\left. + q_4\left(f_\eta + K_a\eta_0\right)^4\right]\right\}\end{aligned} \quad (39)$$

It is obviously that, the phase of signal depends on f_η and η_0. The phase is expanded into the Talyor series, (40) and (41), as shown at the bottom of the next page, the

azimuth modulation rate is analyzed in detail. The expanded phase is shown in (40), which only includes the phase term needed to solve for the parameters.

To correct the azimuth the space variance of the azimuth modulation rate, the coefficients of $\eta_0 f_\eta^2$, $\eta_0^2 f_\eta$, cubic and quadratic phases are equal zero as shown in (41). The reference azimuth position lies in η_0, so the coefficient of $f_\eta \eta_0$ must be -2π. It can be set to $-2\pi/\alpha$ for consistence of the ANCS algorithm, where α has been discussed in [19] and [20].

Solving (41), the paraments are given by (42)

$$\begin{cases} q_2 = K_{a0}(\alpha - 1) \\ Y_3 + \varphi_3 = \frac{K_{a1}(2\alpha-1)}{3K_{a0}^3(\alpha-1)} \\ q_3 = \frac{1}{3}K_{a1}(\alpha - 1) \\ Y_4 + \varphi_4 = \left[2K_{a1}^2(5\alpha - 4) + 3K_{a1}^2 K_{a0}\alpha\right]/12K_{a0}^5(\alpha - 1) \\ q_4 = \left[2K_{a1}^2(5\alpha - 4) - 3K_{a1}^2 K_{a0}\alpha(\alpha - 1)\right]/12K_{a0} \end{cases} \tag{42}$$

After implementing the ANCS operation, we can drive the range Doppler domain signal expression (43), as shown at the bottom of the next page, by Substituting (42) into (39).

According to (43), it is evident that the azimuth location of the target is η_0/α. The second phase term represents the azimuth modulation term, which has been eliminated the azimuth-dependent and is only related to α and K_{a0}. The third and fourth exponential terms are high order phase terms, which need to be compensated before azimuth compression. The remaining exponential terms, which are the remaining phases, can be ignored due to the small magnitude and has negligible effect on the final imaging result.

G. AZIMUTH COMPRESSION

Higher-order terms of f_η in (43) are not compensated. These terms should be considered in the azimuth-matched filter, which is set by referring to the reference target. The azimuth compression function is as

$$\begin{aligned} H_{AC} = &\exp\left\{j\frac{\pi}{\alpha K_{a0}}f_\eta^2\right\}\exp\left\{-j\frac{\pi K_{a1}}{3\alpha(\alpha-1)K_{a0}^3}f_\eta^3\right\} \\ &\cdot\exp\left\{-j\frac{2\alpha(5\alpha-4)K_{a1}^2 + 3K_{a1}^2K_{a0}\alpha^2(2-\alpha)}{12\alpha^4K_{a0}^5(\alpha-1)}f_\eta^4\right\} \end{aligned} \tag{44}$$

Multiplying the signal with the azimuth compression function, we got the azimuth compressed signal.

$$S_{11}(f_\tau, f_\eta) = AP_r(f_\tau)W_a(f_\eta)\exp\left\{-j2\pi\frac{\eta_0}{\alpha}f_\eta\right\} \tag{45}$$

$W_a(f_\eta)$ represent the azimuth envelope after azimuth compression. Converting (45) to azimuth time domain, the

$$\begin{aligned} \Omega(f_\eta, \eta_0) = &\frac{1}{2!}\left\{-2\cdot\frac{2\pi K_{a0}}{K_{a0}+q_2}f_\eta\eta_0\right\} \\ &+\frac{1}{3!}\cdot 3\left\{-\frac{4\pi K_{a1}}{K_{a0}+q_2} + \frac{4\pi K_{a1}K_{a0}}{(K_{a0}+q_2)^2} + \frac{6\pi K_{a0}^2}{(K_{a0}+q_2)^3}\left[(Y_3+\varphi_3)K_{a0}q_2^2 + q_3\right]\right\}\eta_0^2 f_\eta \\ &+\frac{1}{3!}\cdot 3\left\{\frac{2\pi K_{a1}}{(K_{a0}+q_2)^2} + \frac{6\pi K_{a0}}{(K_{a0}+q_2)^3}\left[q_3 - (Y_3+\varphi_3)K_{a0}^2q_2\right]\right\}\eta_0 f_\eta^2 \\ &+\frac{1}{4!}\cdot 6\left\{-\frac{\pi K_{a1}^2\cdot 4}{(K_{a0}+q_2)^3} - \frac{9\pi(Y_3+\varphi_3)K_{a0}^2K_{a1}q_2^2\cdot 4}{(K_{a0}+q_2)^4} + \frac{3\pi K_{a1}q_3(q_2-2K_{a0})\cdot 4}{(K_{a0}+q_2)^4}\right. \\ &\left.+\frac{6\pi K_{a0}^2\cdot 4}{(K_{a0}+q_2)^4}\left[(Y_4+\varphi_4)K_{a0}^2q_2^2 + q_4\right]\right\}f_\eta^2\eta_0^2 \\ &+\frac{1}{4!}\cdot 4\left\{\frac{3\pi K_{a1}\cdot 6}{(K_{a0}+q_2)^3}\left[(Y_3+\varphi_3)K_{a0}^2q_2 - q_3\right] + \frac{4\pi K_{a0}\cdot 6}{(K_{a0}+q_2)^4}\left[q_4 - (Y_4+\varphi_4)K_{a0}^3q_2\right]\right\}\eta_0 f_\eta^3 \\ &+\phi_{res}(q_2, q_3, q_4, f_\eta, \eta_0) \\ &\cdots\cdots \end{aligned} \tag{40}$$

$$\begin{cases} -\frac{2\pi K_{a0}}{K_{a0}+q_2} = -\frac{2\pi}{\alpha} \\ -\frac{2\pi K_{a1}}{K_{a0}+q_2} + \frac{2\pi K_{a1}K_{a0}}{(K_{a0}+q_2)^2} + \frac{3\pi K_{a0}^2}{(K_{a0}+q_2)^3}\left[(Y_3+\varphi_3)K_{a0}q_2^2 + q_3\right] = 0 \\ \frac{\pi K_{a1}}{(K_{a0}+q_2)^2} + \frac{3\pi K_{a0}}{(K_{a0}+q_2)^3}\left[q_3 - (Y_3+\varphi_3)K_{a0}^2q_2\right] = 0 \\ -\frac{\pi K_{a1}^2}{(K_{a0}+q_2)^3} - \frac{9\pi(Y_3+\varphi_3)K_{a0}^2K_{a1}q_2^2}{(K_{a0}+q_2)^4} + \frac{3\pi K_{a1}q_3(q_2-2K_{a0})}{(K_{a0}+q_2)^4} + \frac{6\pi K_{a0}^2}{(K_{a0}+q_2)^4}\left[(Y_4+\varphi_4)K_{a0}^2q_2^2 + q_4\right] = 0 \\ \frac{3\pi K_{a1}}{(K_{a0}+q_2)^3}\left[(Y_3+\varphi_3)K_{a0}^2q_2 - q_3\right] + \frac{4\pi K_{a0}}{(K_{a0}+q_2)^4}\left[q_4 - (Y_4+\varphi_4)K_{a0}^3q_2\right] = 0 \end{cases} \tag{41}$$

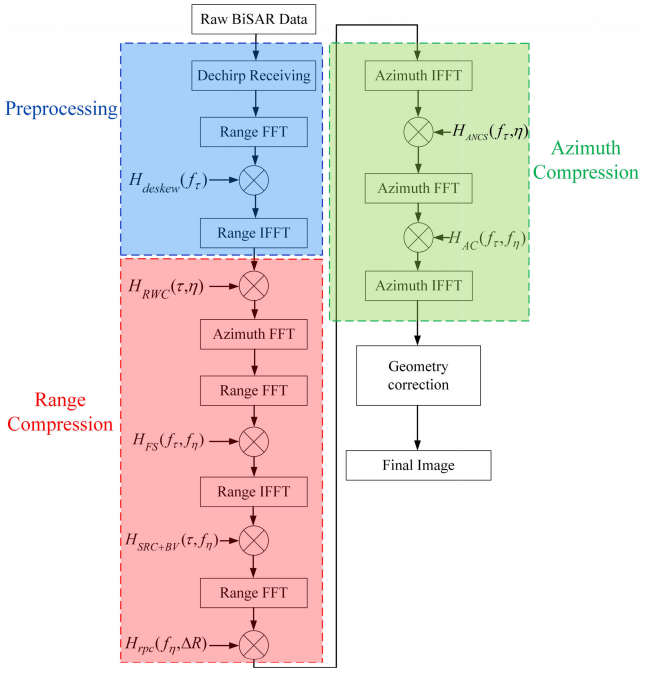

FIGURE 3. Block diagram of the proposed algorithm.

focusing imaging without geometry correction is obtained as

$$S_{12}(f_\tau,\eta) = A\sin c\left\{B_r\left(f_\tau+\frac{K_r}{c}\Delta R\right)\right\} \times \sin c\left\{B_a\left(\eta-\frac{\eta_0}{\alpha}\right)\right\} \tag{46}$$

H. GEOMETRY CORRECTION

The finally location of the targets needs to move $\Delta f = -2K_r/c\Delta R\cdot\sin\theta_e$ in range frequency domain, in which θ_e is determine by k_1, k_2 and k_3 [32]. And a scale transformation by a factor of α is implemented in the azimuth time domain.

The flow diagram of the proposed Bi-EFSA is showed in Figure 3. The preprocessing of dechirp receiving is shaded blue block, the range compression is shaded red block, and the azimuth compression is shaded green block.

I. INVARIANCE REGION ANALYSIS

For each application, the imaging geometry and radar parameters impact the size of the invariance region. There are several factors that restrict the size of the invariance area. Typically, the residual RCM acts as the governing factor. Besides, the ΔR in frequency scaling operation is also an important determinant in proposed algorithm. The following analysis is limited only to the two factors.

$R_T(\Delta x,\Delta y)$, $R_R(\Delta x,\Delta y)$, $\theta_T(\Delta x,\Delta y)$, and $\theta_R(\Delta x,\Delta y)$ specify the slant ranges and squint angles of the transmitter and receiver to a target locating at point $(\Delta x,\Delta y)$, where Δx and Δy are the range and azimuth offsets, respectively, from the reference target $P_0(0,0)$ in the coordinate system after RWC.

According to (8), the residual RCM of a target for an exposure time T_a is given by

$$\begin{aligned}&\Delta R_{RCM}(\Delta x,\Delta y)\\&=\left(1+\frac{\lambda K_r}{c}\left(\tau-\frac{r_{cen}}{c}\right)\right)\\&\quad\times\left\{\begin{array}{l}\left[V_T\sin\left(\theta_T(\Delta x,\Delta y)\right)+V_R\sin\left(\theta_R(\Delta x,\Delta y)\right)\right]T_a\\-\left[V_T\sin\left(\theta_T(0,0)\right)+V_R\sin\left(\theta_R(0,0)\right)\right]T_a\end{array}\right\}\end{aligned} \tag{47}$$

To achieve focusing result, the residual RCM should be maintained to a maximum of one range resolution cell ρ_r inside a processing block. The coefficient is expressed as k_{rcm}, which should be less than 1. The maximum range deviation Δx_{rcm} from reference target P_0 is as follows:

$$\Delta R_{RCM}(\Delta x_{rcm},0) < k_{rcm}\rho_r \tag{48}$$

While the maximum azimuth deviation Δy_{rcm} from reference target P_0 is as follows. ρ_a is one azimuth resolution cell.

$$\Delta R_{RCM}(0,\Delta y_{rcm}) < k_{rcm}\rho_a \tag{49}$$

In section III.B., $C(f_\eta)$ is ignored due to insignificant small. Though they have a similar form, they are the combinations of coefficients in different orders of ΔR. The phase $\left|-2\pi\cdot K_r/c\cdot C(f_\eta)\Delta R^2(\Delta x,\Delta y)\right|$ should less than $\pi/4$.

$$2\pi\frac{K_r}{c}\left|C(f_\eta)\Delta R^2(\Delta x,\Delta y)\right| < \frac{\pi}{4} \tag{50}$$

The maximum range deviation Δx_{rcm} from reference target P_0 is as follows:

$$2\pi\frac{K_r}{c}\left|C(f_\eta)\Delta R^2(\Delta x,0)\right| < \frac{\pi}{4} \tag{51}$$

$$\begin{aligned}S_{10}(f_\tau,f_\eta) &= AP_r(f_\tau)\exp\left\{-j2\pi\frac{\eta_0}{\alpha}f_\eta\right\}\exp\left\{-j\frac{\pi}{\alpha K_{a0}}f_\eta^2\right\}\exp\left\{j\frac{\pi K_{a1}}{3\alpha(\alpha-1)K_{a0}^3}f_\eta^3\right\}\\&\times\exp\left\{j\frac{2\alpha(5\alpha-4)K_{a1}^2+3K_{a1}^2K_{a0}\alpha^2(2-\alpha)}{12\alpha^4K_{a0}^5(\alpha-1)}f_\eta^4\right\}\exp\left\{j\frac{\pi K_{a0}(\alpha-1)}{\alpha}\eta_0^2\right\}\exp\left\{j\frac{\pi K_{a1}(\alpha-1)}{3\alpha}\eta_0^3\right\}\\&\times\left\{j\pi\left[-2K_{a1}^2K_{a0}^4\alpha^2(\alpha-1)^3+\frac{1}{6}K_{a1}^2K_{a0}^3(5\alpha-4)\left((\alpha-1)^3+1\right)+\frac{1}{4}K_{a1}^2K_{a0}^4\alpha^2(\alpha-1)(\alpha-2)\right]\eta_0^4\right\}\end{aligned} \tag{43}$$

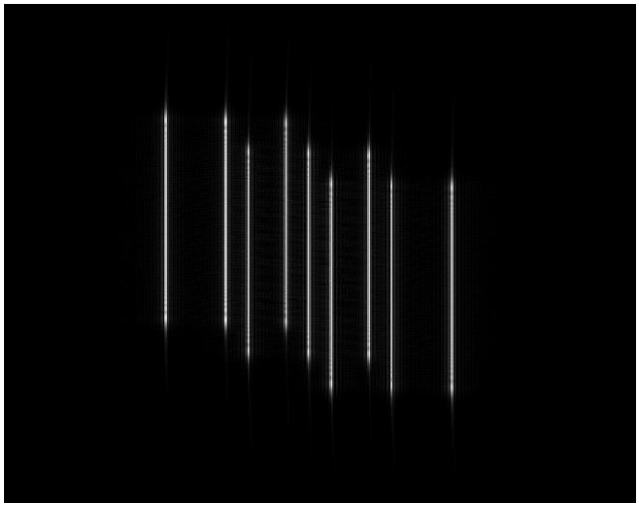

FIGURE 4. Simulation results of Point targets after FS operation.

While the maximum azimuth deviation Δy_{rcm} from reference target P_0 is as follows:

$$2\pi \frac{K_r}{c} \left| C(f_\eta) \Delta R^2 (0, \Delta y) \right| < \frac{\pi}{4} \tag{52}$$

Finally, the range invariance region size is founded as:

$$\Delta X_{ir} = 2 \cdot \min \{\Delta x_{rcm}, \Delta x\} \tag{53}$$

and the azimuth invariance region size is founded as:

$$\Delta Y_{ir} = 2 \cdot \min \{\Delta y_{rcm}, \Delta y\} \tag{54}$$

IV. RESULTS

A. SIMULATION AND ANALYSIS OF PHASE FUNCTION

The phase expression of azimuth frequency in section III-A. before FS operation is expanded into the function of fast time τ. We omit the fourth-order phase term in phase expand expression (13), and analysis as follow. The different orders of phase expressions are shown in Figure 4. The quartic phase term is much smaller than the other order phases and can be ignored. And for the BiSAR with high squint angles, the major component for the azimuth processing is the primary phase term. The simulations for different orders of phases based on the GEO transmitter are shown in Figure 5. Compared with Figure 4, the primary phase term based on the GEO transmitter is significantly large due to the GEO transmitter. The third-order phase based on the GEO transmitter is around $\pi/4$ which need to be compensated by (15). The fourth-order phase terms for different transmitters are similar and much smaller than the other order phases despite the type of transmitter. According to simulations, it should be noticed that even when the transmitter is settled on airplanes, LEO, or GEO satellites, the fourth-order phase term is still small enough to be ignored and the only difference between them is the magnitude of the first-order phase. Based on the dechirp receiving, the sampling frequency in the receiving system is largely reduced, and the efficiency

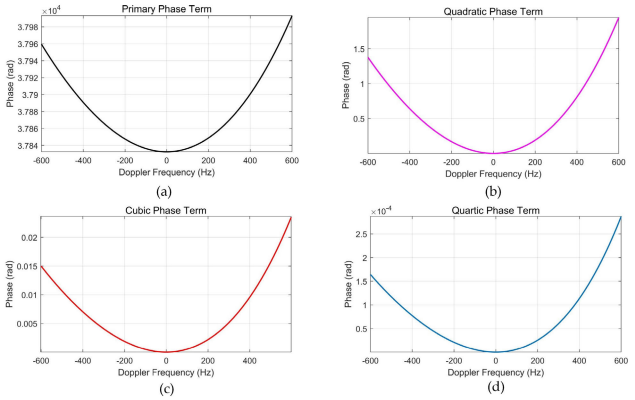

FIGURE 5. The imaging results of point targets before geometry correction by Bi-EFSA.

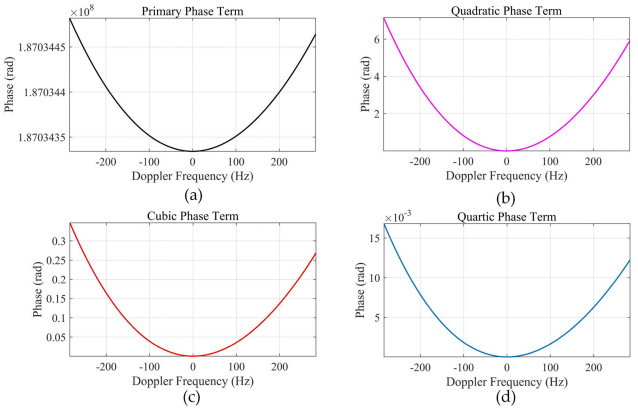

FIGURE 6. The imaging results of point targets before geometry correction by NLCS algorithm.

of the focusing procedure for such a BiSAR configuration is improved. Then, the RWC is carried out in the 2-D time domain, which significantly reduces the serious coupling between the azimuth and range caused by range walk. With the operation of frequency scaling, the space variance of the range curvatures is reduced, and the range curvatures of all point targets are corrected to be consistent at once as shown in Figure 4 (simulation results of point targets based on Table 1 parameters with 400 m in both range and azimuth directions).

B. SIMULATION RESULTS OF POINTS TARGETS

As analysis in the section IV-A., the platform of transmitter is not the main challenge for the high squint angle BiSAR imaging. As a result, the airborne bistatic with high squint angles was employed for simulation to verify the accuracy and imaging performance of the proposed algorithm. The experiment parameters are shown in the Table 1.

The spatial distribution of point targets is in the x-y plane with a 100 m distance between adjacent both in x and y directions. The scene size is assumed to be 200 m both in range and azimuth directions which is sufficient for surveillance of key regions.

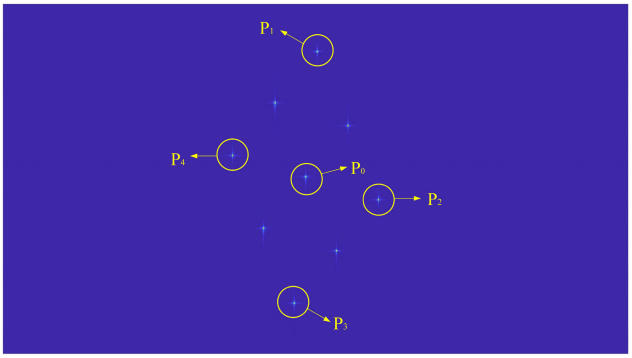

FIGURE 7. Simulation results for different orders of phase based on airborne transmitter.

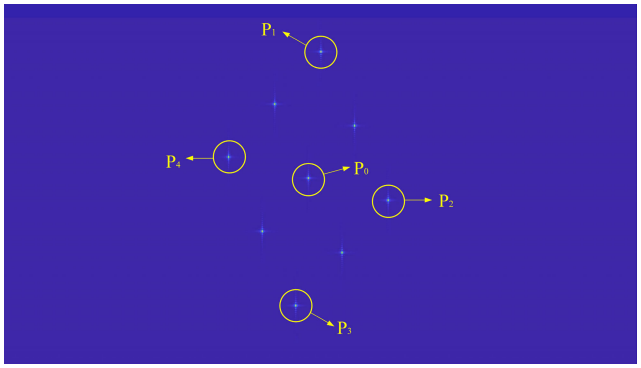

FIGURE 8. Simulation results for different orders of phase based on GEO transmitter.

The imaging results for the scene processed by the Bi-EFSA are shown in Figure 7, in which all the targets are well focused. The value of α coefficient for the ANCS operation in azimuth compression processing is set to be 0.65, which is enough to process the small key region [18], [33]. And the energy of each target in the range frequency domain and azimuth time domain is gathered into corresponding bins in both the range and azimuth directions. In addition, the simulation results of point target array by NLCS algorithm before geometry correction are also given in Figure 8, in which all the targets are well focused. The geometry correction is needed when processing the echo data of area targets to get a final image that matches the real area. In Figures 9(a) and (b) show the imaging results after geometry by the proposed Bi-EFSA and the NLCS, respectively.

The BP algorithm's imaging results of point targets are also simulated and given in Figure 10. Since the BP algorithm calculates point-by-point to obtain focusing imaging, the imaging results of point targets are similar to those of the other two algorithms after geometry correction. The BP algorithm simulation provides imaging results that approximate the ideal image for reference. Compared with the BPA simulation results, the effectiveness of the proposed algorithm is proved.

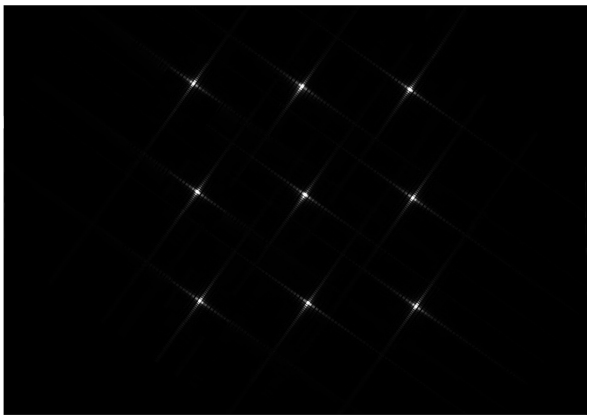

(a)

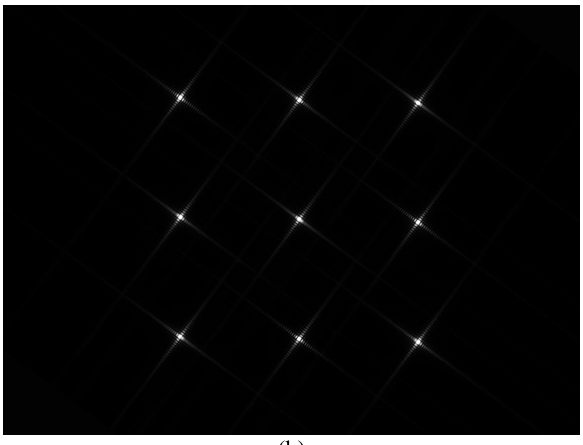

(b)

FIGURE 9. The imaging results after geometry correction. (a) by Bi-EFSA; (b) by NLCS algorithm.

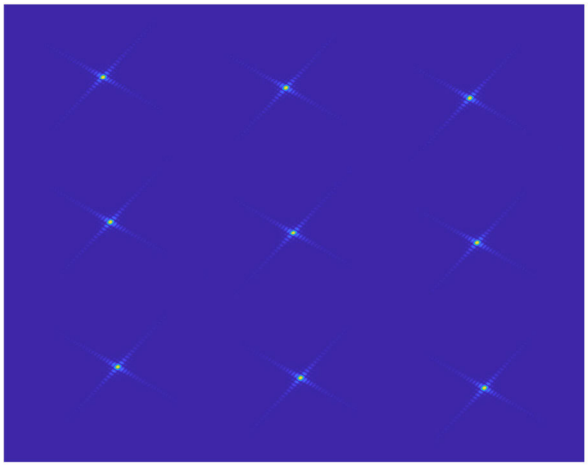

FIGURE 10. The imaging results of point targets by BP algorithm.

Based on the parameters in Table 1 and the configuration of high squint angle BiSAR, the theoretical resolution values are 1.40 m in azimuth and 2.11 m in range. The targets P0, P1, and P2 are extracted from the scene and up sampled to obtain the detail imaging results, which are

TABLE 2. Simulated Results of the selected Targets by Bi-EFSA, NLCSA and BP.

Point Target	Algorithm	Range			Azimuth		
		Resolution (m)	PSLR (dB)	ISLR (dB)	Resolution (m)	PSLR (dB)	ISLR (dB)
Target P0	Bi-EFSA	2.11	-13.70	-10.20	1.44	-12.12	-10.19
	NLCSA	3.04	-13.27	-10.08	2.44	-12.56	-10.63
	BPA	2.11	-12.53	-10.54	1.41	-13.35	-12.84
Target P1	Bi-EFSA	2.11	-13.12	-10.55	1.50	-11.69	-10.09
	NLCSA	3.04	-13.78	-10.41	2.44	-12.32	-10.13
	BPA	2.11	-12.45	-10.52	1.41	-13.34	-12.84
Target P2	Bi-EFSA	2.11	-13.68	-10.21	1.51	-11.28	-10.01
	NLCSA	3.04	-13.49	-10.44	2.45	-12.43	-10.35
	BPA	2.11	-12.52	-10.50	1.42	-13.35	-12.85

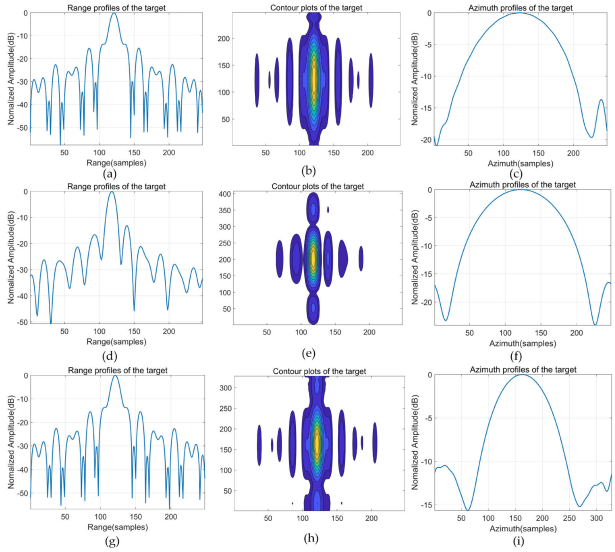

FIGURE 11. Detailed imaging results of three targets by Bi-EFSA. (a) Range slice of Target P0. (b) Contourplots of Target P0. (c) Azimuth slice of Target P0. (d) Range slice of Target P1. (e) Contourplots of Target P1. (f) Azimuth slice of Target P1. (g) Range slice of Target P2. (h) Contourplots of Target P2. (i) Azimuth slice of Target P2.

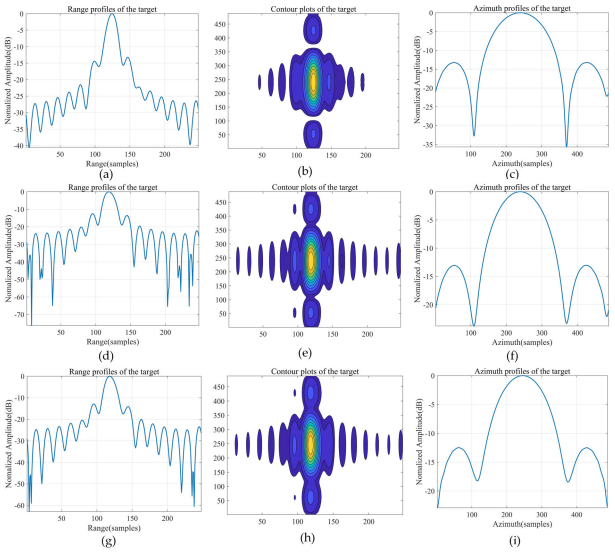

FIGURE 12. Detailed imaging results of three targets by NLCS algorithm. (a) Range slice of Target P0. (b) Contourplots of Target P0. (c) Azimuth slice of Target P0. (d) Range slice of Target P1. (e) Contourplots of Target P1. (f) Azimuth slice of Target P1. (g) Range slice of Target P2. (h) Contourplots of Target P2. (i) Azimuth slice of Target P2.

demonstrated in Figures 11b, e, and h. Additionally, the slices of each target in range and azimuth directions are shown in Figures 11a, c, d, f, g, and i, respectively. The corresponding measured peak sidelobe ratio (PSLR) and integrated sidelobe ratio (ISLR) are calculated and listed in Table 2. The target P0 is taken as an example, the azimuth resolution is 1.44 meters, and the range resolution is 2.11 meters. In the azimuth direction, the PSLR is 12.12 dB, and the ISLR is 10.19 dB. While in the range direction, the PSLR is 13.70 dB, and the ISLR is 10.20 dB. The synthetic time is 4 seconds.

For the imaging results simulated by NLCS algorithm, the targets P0, P1, and P2 are extracted from the scene and up sampled to obtain the detail imaging results, which are demonstrated in Figures 12b, e, and h. Additionally, the slices of each target in range and azimuth directions are shown in Figures 12a, c, d, f, g, and i, respectively. The corresponding measured peak sidelobe ratio (PSLR) and integrated sidelobe ratio (ISLR) are calculated and listed in Table 2. The target P0 is taken as an example, the azimuth resolution is 2.44 meters, and the range resolution is 3.04 meters. In the azimuth direction, the PSLR is 12.56 dB, and the ISLR is 10.63 dB. While in the range direction, the PSLR is 13.27 dB, and the ISLR is 10.08 dB. The synthetic time is 4 seconds.

To further verify the algorithm's effectiveness, the imaging results simulated by the BP algorithm, in which the targets P0, P1, and P2 are extracted from the scene and up sampled to obtain the detailed imaging results, are demonstrated in Figures 13b, e, and h. Additionally, the slices of each target in range and azimuth directions are shown in Figures 13a, c, d, f, g, and i, respectively. The corresponding

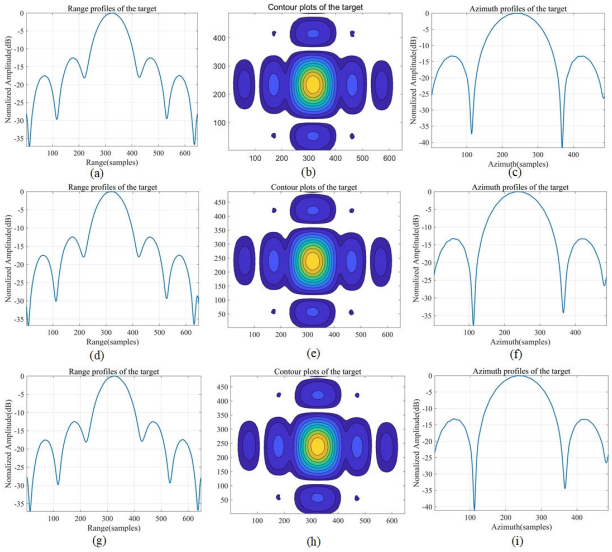

FIGURE 13. Detailed imaging results of three targets by BP algorithm. (a) Range slice of Target P0. (b) Contourplots of Target P0. (c) Azimuth slice of Target P0. (d) Range slice of Target P1. (e) Contourplots of Target P1. (f) Azimuth slice of Target P1. (g) Range slice of Target P2. (h) Contourplots of Target P2. (i) Azimuth slice of Target P2.

measured peak sidelobe ratio (PSLR) and integrated sidelobe ratio (ISLR) are calculated and listed in Table 2 as the benchmarks for the proposed algorithm. The target P0 is taken as an example, the azimuth resolution is 1.41 meters, and the range resolution is 2.11 meters. In the azimuth direction, the PSLR is 13.35 dB, and the ISLR is 12.84 dB. While in the range direction, the PSLR is 12.53 dB, and the ISLR is 10.54 dB. The synthetic time is still 4 seconds.

Compared to the simulation results of the NLCS algorithm, the resolutions in range and azimuth of proposed Bi-EFSA is better. This is caused by the high squint angle bistatic configuration. In the NLCS algorithm, a cubic phase perturbation function for the bistatic SAR is performed to identify the azimuth frequency modulation (FM) rates of all targets at the same range gate [16]. The tuning effect of perturbation function is limited. For highly squint angle, higher order range-azimuth coupling leads to inaccurate focusing performance [20]. According to the analysis of reference [18], the NLCS algorithm can achieved good results for squint angles up to 40° for the C-band in monostatic SAR. Under the same squint angle, the imaging performance of non-parallel bistatic SAR will be worse due to its complex configuration. Thus, the proposed Bi-EFSA obtained better resolutions than the NLCS algorithm. In addition, the processing times of the NLCS algorithm and the proposed Bi-EFSA on the same computer are 73.22 s and 12.93 s, respectively. The proposed Bi-EFSA obtains better computational efficiency due to non-interpolation operations.

As the benchmarks for SAR imaging, the simulation results obtained by the BP algorithm achieved good focusing performance both in the range and azimuth directions. In the proposed algorithm, the range walk correction and the FS operation processed the dechirp received signal of Bistatic SAR with high squint angles to achieve good focusing performance in the range direction, ANCS operation. Considering the computational efficiency, the focusing performance of the proposed algorithm is as the BP algorithm did. The focusing performance in the azimuth is not as accurate as the BP algorithm due to the approximation of the azimuth frequency modulation in acceptable. According to the comparations in Table 2, the simulation results verified the effectiveness and accuracy of the proposed algorithm.

C. EXTENDED-SCENE SIMULATION EXPERIMENT

An extended-scene simulation experiment, in which the scattering coefficients of the scene are from an actual SAR image, is simulated by proposed Bi-EFSA and the NLCS algorithm. The actual SAR images are based on the scene data of Hengdian, Yiwu, Zhejiang Province, admitted by GF3 in the Xi'an Branch of the China Academy of Space Technology in 2020. The actual SAR imaging scenes is shown in Figures 14b and e. The simulation results of two scenes by Bi-EFSA and NLCS algorithm are shown in Figures 14a, c, d and f. The simulations are based on the same experiment parameters shown same experiment parameters shown in the Table 1. The focused imaging performance of the proposed algorithm is comparable to that of the NLCS algorithm. It should be noted that the GF-3 was in slide spotlight mode, with a bandwidth of 240 MHz. For limitations based on computer power, the simulations by Bi-EFSA and NLCS take 80 MHz as the bandwidth to verify the algorithm's effectiveness. This is also why the resolution of the simulation result is worse than the actual imaging result of the scene. With the same parameters and scattering coefficients of the scenes, Bi-EFSA obtains a better resolution and a slightly better focusing performance in some areas. It is evident that under the same simulation parameter settings, the proposed algorithm has better imaging performance, obtaining more explicit ground area boundary information and contour features of the targets. For scene 1 in Figure 13b, the imaging performance of the proposed algorithm in Figure 13a is better. In the left circle, the two algorithm in Figure 14a is better. In the left circle, the two bridges can be distinguished. In the right circle, the outlines and demarcation of the two small islands can be more easily discerned. For scene 2 in Figure 14e, the imaging performance of the proposed algorithm in Figure 14d achieved better resolutions both in the range and azimuth directions. In the circle below, the details and boundaries of the airport terminal are more clearly defined.

To further illustrate the algorithm's effectiveness, the signal bandwidth was changed to match more closely that of the original SAR image by 250 MHz, and simulated experiments of extended scenes of Bi-EFSA were added while keeping other parameters unchanged. The imaging result is given in Figure 15, in which higher resolution and better focusing performance are obtained. For instance, the bridge connecting two small islands is imaged and has clear boundaries. The effectiveness and advantages of the algorithm are more intuitively demonstrated.

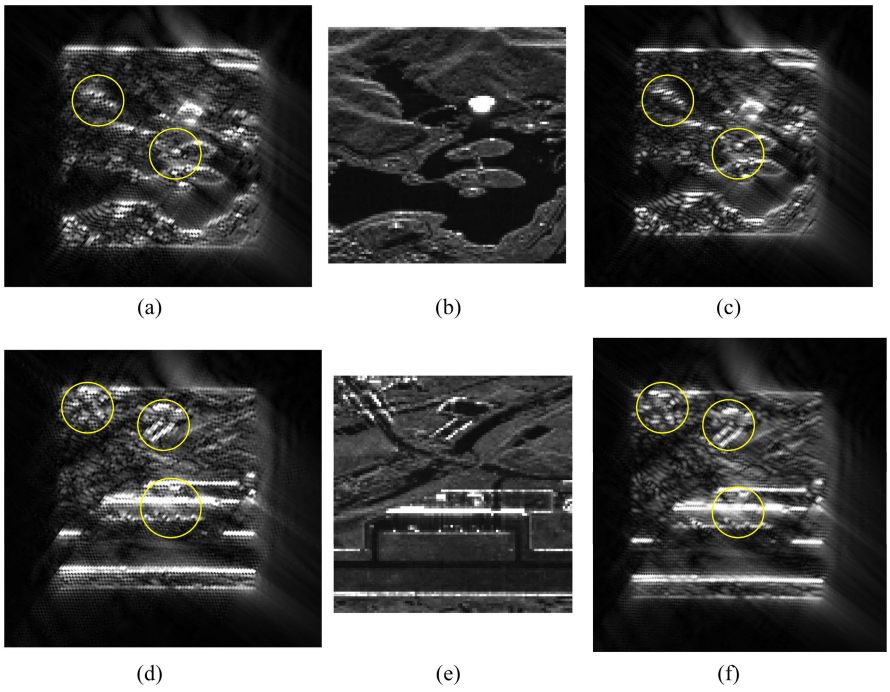

FIGURE 14. The simulation results of two scenes by Bi-EFSA and NLCS algorithm. (a) Focusing Image of scene 1 by Bi-EFSA; (b) Actual SAR image of scene 1; (c) Focusing Image of scene 1 by NLCS algorithm; (d) Focusing Image of scene 2 by Bi-EFSA; (e) Actual SAR image of scene 2; (f) Focusing Image of scene 2 by NLCS algorithm.

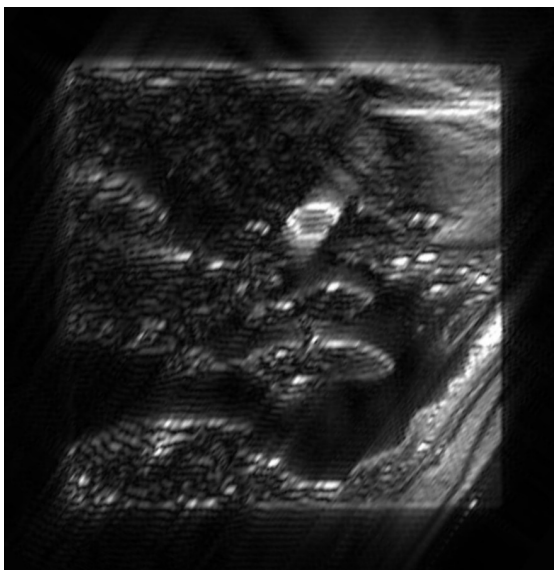

FIGURE 15. The simulation results of scene by Bi-EFSA with 250 MHz bandwidth.

D. OPERATION COMPLEXITY ANALYSIS

According to the algorithm flowcharts, the operation complexity of the proposed algorithm is analyzed. Assuming that the dimensionality of the Raw data is $N_a \times N_r$, N_r is the number of range samples, N_a is the number of azimuth samples. Based on the analysis in [34], for each FFT the operation complexity is derived as $5N_rN_a\log_2(N_{r/a})$, while the complex multiplication takes $6N_rN_a$. Therefore, the computational complexity of the proposed algorithm can be derived as

$$S = 25N_rN_a\log_2(N_r) + 20N_rN_a\log_2(N_a) + 48N_rN_a \quad (55)$$

V. CONCLUSION

In this paper, a bistatic extended frequency scaling algorithm (Bi-EFSA) is proposed to deal with the dechirp received signal for bistatic SAR with high squint angle. The echo of the imaging scene centroid is used as the reference signal to obtain better focus results. The range walk correction in the 2-D time domain reduces the space variance of the range curvatures and removals the serious coupling between range and azimuth caused by the high squint angle, which is the first step of Bi-EFSA. For azimuth processing, the space variance of the azimuth frequency modulation rate, introduced by the range walk correction step, is effectively corrected by implementing the azimuth nonlinear chirp scaling (ANCS) operation. At last, the focused results in the range frequency and azimuth time domain are obtained by the azimuth compression. The invariance region analysis is also carried out. The algorithm can deal with the BiSAR with high squint angles and achieves good focusing performance. It also obtains better computational efficiency compared to the BPA, RDA, NLCS, and ωKA, which need interpolation operations. Finally, the simulated results compared to the NLCS algorithm and BP algorithm, and the extended-scene simulation experiment validate the effectiveness of the proposed method.

REFERENCES

[1] O. Loffeld, H. Nies, V. Peters, and S. Knedlik, "Models and useful relations for bistatic SAR processing," *IEEE Trans. Geosci. Remote Sens.*, vol. 42, no. 10, pp. 2031–2038, Oct. 2004, doi: 10.1109/TGRS.2004.835295.

[2] S. Duque, P. Lopez-Dekker, and J. J. Mallorqui, "Single-pass bistatic SAR interferometry using fixed-receiver configurations: Theory and experimental validation," *IEEE Trans. Geosci. Remote Sens.*, vol. 48, no. 6, pp. 2740–2749, Jun. 2010, doi: 10.1109/TGRS.2010.2041063.

[3] L. Maslikowski, P. Samczynski, M. Baczyk, P. Krysik, and K. Kulpa, "Passive bistatic SAR imaging—Challenges and limitations," *IEEE Aerosp. Electron. Syst. Mag.*, vol. 29, no. 7, pp. 23–29, Jul. 2014, doi: 10.1109/MAES.2014.130141.

[4] G. Krieger and A. Moreira, "Spaceborne bi- and multistatic SAR: Potential and challenges," *IEE Proc.-Radar, Sonar Navigat.*, vol. 153, no. 3, pp. 184–198, Jun. 2006, doi: 10.1049/ip-rsn:20045111.

[5] M. Rodriguez-Cassola, S. V. Baumgartner, G. Krieger, A. Nottensteiner, R. Horn, U. Steinbrecher, R. Metzig, M. Limbach, P. Prats, J. Fischer, M. Schwerdt, and A. Moreira, "Bistatic spaceborne-airborne experiment TerraSAR-X/F-SAR: Data processing and results," in *Proc. IEEE Int. Geosci. Remote Sens. Symp.*, Jul. 2008, p. 451.

[6] I. Walterscheid, T. Espeter, A. Brenner, J. Klare, J. Ender, H. Nies, R. Wang, and O. Loffeld, "Bistatic SAR experiments with PAMIR and TerraSAR-X-setup, processing, and image results," *IEEE Trans. Geosci. Remote Sens.*, vol. 48, no. 8, pp. 3268–3279, Aug. 2010.

[7] G. W. Davidson and I. Cumming, "Signal properties of spaceborne squint-mode SAR," *IEEE Trans. Geosci. Remote Sens.*, vol. 35, no. 3, pp. 611–617, May 1997, doi: 10.1109/36.581976.

[8] S. Quegan, "Spotlight synthetic aperture radar: Signal processing algorithms," *J. Atmos. Solar-Terr. Phys.*, vol. 59, pp. 597–598, Mar. 1997, doi: 10.1016/S1364-6826(97)83336-6.

[9] H. An, J. Wu, Z. He, Z. Li, and J. Yang, "Geosynchronous spaceborne–airborne multichannel bistatic SAR imaging using weighted fast factorized backprojection method," *IEEE Geosci. Remote Sens. Lett.*, vol. 16, no. 10, pp. 1590–1594, Oct. 2019, doi: 10.1109/LGRS.2019.2902036.

[10] Y. Ding and D. C. J. Munson, "A fast back-projection algorithm for bistatic SAR imaging," in *Proc. Int. Conf. Image Process.*, 2002, pp. 1–4, doi: 10.1109/ICIP.2002.1039984.

[11] Y. F. Shao, R. Wang, Y. K. Deng, Y. Liu, R. Chen, G. Liu, and O. Loffeld, "Fast backprojection algorithm for bistatic SAR imaging," *IEEE Geosci. Remote Sens. Lett.*, vol. 10, no. 5, pp. 1080–1084, Sep. 2013, doi: 10.1109/LGRS.2012.2230243.

[12] Y. L. Neo, F. H. Wong, and I. G. Cumming, "Processing of azimuth-invariant bistatic SAR data using the range Doppler algorithm," *IEEE Trans. Geosci. Remote Sens.*, vol. 46, no. 1, pp. 14–21, Jan. 2008.

[13] R. Wang, O. Loffeld, and Y. L. Neo, "Focusing bistatic SAR data in airborne/stationary configuration," *IEEE Trans. Geosci. Remote Sens.*, vol. 48, no. 1, pp. 452–465, Jan. 2010, doi: 10.1109/tgrs.2009.2027700.

[14] H. Zhong and X. Liu, "An effective focusing approach for azimuth invariant bistatic SAR processing," *Signal Process.*, vol. 90, no. 1, pp. 395–404, Jan. 2010, doi: 10.1016/j.sigpro.2009.07.005.

[15] S. Chen, Y. Yuan, S. Zhang, H. Zhao, and Y. Chen, "A new imaging algorithm for forward-looking missile-borne bistatic SAR," *IEEE J. Sel. Topics Appl. Earth Observ. Remote Sens.*, vol. 9, no. 4, pp. 1543–1552, Apr. 2016, doi: 10.1109/JSTARS.2015.2507260.

[16] F. H. Wong, I. G. Cumming, and Y. L. Neo, "Focusing bistatic SAR data using the nonlinear chirp scaling algorithm," *IEEE Trans. Geosci. Remote Sens.*, vol. 46, no. 9, pp. 2493–2505, Sep. 2008, doi: 10.1109/TGRS.2008.917599.

[17] X. Qiu, D. Hu, and C. Ding, "An improved NLCS algorithm with capability analysis for one-stationary BiSAR," *IEEE Trans. Geosci. Remote Sens.*, vol. 46, no. 10, pp. 3179–3186, Oct. 2008, doi: 10.1109/TGRS.2008.921569.

[18] G. Sun, X. Jiang, M. Xing, Z.-J. Qiao, Y. Wu, and Z. Bao, "Focus improvement of highly squinted data based on azimuth nonlinear scaling," *IEEE Trans. Geosci. Remote Sens.*, vol. 49, no. 6, pp. 2308–2322, Jun. 2011, doi: 10.1109/TGRS.2010.2102040.

[19] D. Li, G. Liao, W. Wang, and Q. Xu, "Extended azimuth nonlinear chirp scaling algorithm for bistatic SAR processing in high-resolution highly squinted mode," *IEEE Geosci. Remote Sens. Lett.*, vol. 11, no. 6, pp. 1134–1138, Jun. 2014, doi: 10.1109/LGRS.2013.2288292.

[20] D. An, X. Huang, T. Jin, and Z. Zhou, "Extended nonlinear chirp scaling algorithm for high-resolution highly squint SAR data focusing," *IEEE Trans. Geosci. Remote Sens.*, vol. 50, no. 9, pp. 3595–3609, Sep. 2012, doi: 10.1109/TGRS.2012.2183606.

[21] Z. Sun, J. Wu, Z. Li, Y. Huang, and J. Yang, "Highly squint SAR data focusing based on keystone transform and azimuth extended nonlinear chirp scaling," *IEEE Geosci. Remote Sens. Lett.*, vol. 12, no. 1, pp. 145–149, Jan. 2015, doi: 10.1109/LGRS.2014.2329554.

[22] B. Liu, T. Wang, Q. Wu, and Z. Bao, "Bistatic SAR data focusing using an omega-K algorithm based on method of series reversion," *IEEE Trans. Geosci. Remote Sens.*, vol. 47, no. 8, pp. 2899–2912, Aug. 2009, doi: 10.1109/TGRS.2009.2017522.

[23] R. Wang O. Loffeld, H. Nies, and J. H. G. Ender, "Focusing space-borne/airborne hybrid bistatic SAR data using wavenumber-domain algorithm," *IEEE Trans. Geosci. Remote Sens.*, vol. 47, no. 7, pp. 2275–2283, Jul. 2009, doi: 10.1109/TGRS.2008.2010852.

[24] T. Zeng, F. Liu, C. Hu, and T. Long, "Image formation algorithm for asymmetric bistatic SAR systems with a fixed receiver," *IEEE Trans. Geosci. Remote Sens.*, vol. 50, no. 11, pp. 4684–4698, Nov. 2012, doi: 10.1109/TGRS.2012.2190937.

[25] Y. Li, Z. Zhang, M. Xing, and Z. Bao, "Bistatic spotlight SAR processing using the frequency-scaling algorithm," *IEEE Geosci. Remote Sens. Lett.*, vol. 5, no. 1, pp. 48–52, Jan. 2008, doi: 10.1109/LGRS.2007.907306.

[26] M. Antoniou, M. Cherniakov, and C. Hu, "Space-surface bistatic SAR image formation algorithms," *IEEE Trans. Geosci. Remote Sens.*, vol. 47, no. 6, pp. 1827–1843, Jun. 2009, doi: 10.1109/TGRS.2008.2007571.

[27] J. Mittermayer, A. Moreira, and O. Loffeld, "Spotlight SAR data processing using the frequency scaling algorithm," *IEEE Trans. Geosci. Remote Sens.*, vol. 37, no. 5, pp. 2198–2214, Sep. 1999, doi: 10.1109/36.789617.

[28] C. Shichao, L. Ming, Y. Lei, X. Mengdao, and B. Zheng, "Bistatic SAR data focusing using an analytical spectrum based frequency scaling algorithm in tandem configuration," in *Proc. IEEE CIE Int. Conf. Radar*, Oct. 2011, pp. 1684–1687, doi: 10.1109/CIE-Radar.2011.6159892.

[29] D. Zhu, M. Shen, and Z. Zhu, "Some aspects of improving the frequency scaling algorithm for dechirped SAR data processing," *IEEE Trans. Geosci. Remote Sens.*, vol. 46, no. 6, pp. 1579–1588, Jun. 2008, doi: 10.1109/TGRS.2008.916468.

[30] Y. L. Neo, F. Wong, and I. G. Cumming, "A two-dimensional spectrum for bistatic SAR processing using series reversion," *IEEE Geosci. Remote Sens. Lett.*, vol. 4, no. 1, pp. 93–96, Jan. 2007, doi: 10.1109/LGRS.2006.885862.

[31] Y. Wang, J. Li, F. Xu, and J. Yang, "A new nonlinear chirp scaling algorithm for high-squint high-resolution SAR imaging," *IEEE Geosci. Remote Sens. Lett.*, vol. 14, no. 12, pp. 2225–2229, Dec. 2017, doi: 10.1109/LGRS.2017.2758386.

[32] Z. Sun, J. Wu, Z. Li, H. An, and X. He, "Geosynchronous spaceborne-airborne bistatic SAR data focusing using a novel range model based on one-stationary equivalence," *IEEE Trans. Geosci. Remote Sens.*, vol. 59, no. 2, pp. 1214–1230, Feb. 2021, doi: 10.1109/TGRS.2020.3002900.

[33] D. X. An, Z.-M. Zhou, X.-T. Huang, and T. Jin, "A novel imaging approach for high resolution squinted spotlight SAR based on the deramping-based technique and azimuth NLCS principle," *Prog. Electromagn. Res.*, vol. 123, pp. 485–508, 2012, doi: 10.2528/PIER11112110.

[34] D. Li, H. Lin, H. Liu, G. Liao, and X. Tan, "Focus improvement for high-resolution highly squinted SAR imaging based on 2-D spatial-variant linear and quadratic RCMs correction and azimuth-dependent Doppler equalization," *IEEE J. Sel. Topics Appl. Earth Observ. Remote Sens.*, vol. 10, no. 1, pp. 168–183, Jan. 2017, doi: 10.1109/JSTARS.2016.2569561.

HAOHUA ZHANG received the B.S. and M.S. degrees from Xidian University, Xi'an, China, in 2013 and 2017, respectively. He is currently pursuing the Ph.D. degree with the Xi'an Branch, China Academy of Space Technology, Xi'an.

His main research interests include bistatic SAR systems and their imaging algorithms, GEO SAR imaging algorithms, and signal processing.

WEIHUA ZUO was born in Hengyang, Hunan, China. He received the Ph.D. degree from the University of Electronic Science and Technology of China, Chengdu, China, in 2015. He has been with the Xi'an Branch, China Academy of Space Technology, Xi'an, since 2015. His main research interests include the Bistatic systems and their imaging algorithms, high-resolution wide-swath SAR imaging systems, patterns and signal processing methods.

BO LIU was born in Enshi, Hubei, in 1963. He is currently a professor, a senior engineer, and a Ph.D. supervisor. He is also an Aerospace Technology Expert with the Xi'an Branch, China Academy of Space Technology, Xi'an. His research interest includes satellite system design.

CAIPIN LI received the B.S. degree from Air Force Engineering University, Xi'an, China, the M.S. degree from the Xi'an Institute of Space Radio Technology, Xi'an, and the Ph.D. degree from Northwest Polytechnic University, Xi'an. He is a Professor with the Xi'an Branch, China Academy of Space Technology, Xi'an. His main research interest includes high-orbit SAR imaging.

DONGTAO LI received the B.S. degree in mechatronic engineering from Dalian Jiaotong University, Dalian, China, in 2006, and the Ph.D. degree in mechatronic engineering from the Beijing Institute of Technology, Beijing, China, in 2014. His Ph.D. dissertation focused on intelligent signal processing. In 2014, he joined the Xi'an Branch, China Academy of Space Technology, Xi'an. His current research interests include geosynchronous synthetic aperture radar (SAR) system design and experiments, bistatic SAR systems and experiments, and bistatic SAR signal processing.

CHONGDI DUAN received the B.S. degree from the Harbin Institute of Technology, Harbin, China, in 1994, and the M.S. degree from the School of Electronic Engineering, Xidian University, Xi'an, China, in 2005. He is currently pursuing the Ph.D. degree with Beijing Institute of Technology, Beijing, China. He is also a Professor with the National Key Laboratory of Science and Technology on Space Microwave, Xi'an Branch, China Academy of Space Technology, Xi'an. His research interests include adaptive and array signal processing, and high-speed real-time signal processors.